Article

Optimization of the Countercurrent Continuous Reforming Process Based on Equation-Oriented Modeling and the SQP Algorithm

Hongbo Jiang,* Zhenming Li, Yun Sun, Shubao Jiang, and Jianhui Tian

Read Online

ACCESS | Metrics & More | Article Recommendations | SI Supporting Information

ABSTRACT: Catalytic reforming is a key technology in the petroleum refining and petrochemical industry. In recent years, countercurrent continuous reforming has put forward and practiced the new concept of matching the activity of the catalyst with the difficulty of the reaction. Based on the equation-oriented method, the steady-state model for the reactor-regenerator section of countercurrent continuous reforming was established, including the reactor module, the regenerator module, the compressor model, the heat exchanger model, the heating furnace model, and the oil property model. The inlet and outlet of each module are connected according to the actual technological process, and the model conforms to the requirement of real-time optimization (RTO). The sequential quadratic programming (SQP) algorithm is used for calculation in this study. The model is calibrated to make the calculated value more consistent with the actual value. The model simulation showed the trend of the reforming reaction and the difference between countercurrent reforming and cocurrent reforming. Finally, the process model was optimized for different goals such as the yield of aromatics, the yield of high-octane gasoline, and the yield of C_7^+ aromatics. These results indicate that the established model can simulate the actual industrial process, which can meet the requirements of RTO, and obtain considerable profits for different optimization objectives.
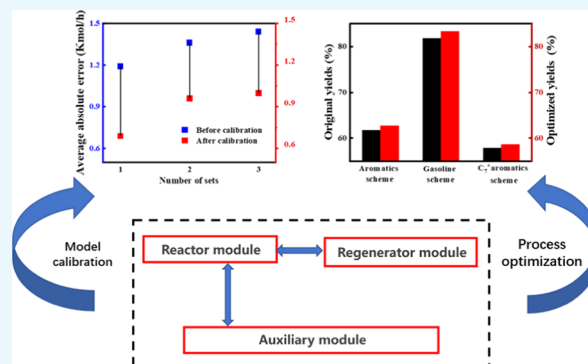
1. INTRODUCTION

Refining and petrochemical industries are important because they provide energy and chemicals, especially transportation fuels and raw organic chemical materials.[1] The development of process simulation for these petroleum-related processes will provide better guidance for plant operations and lead to better economic benefits. The process simulation technology originated from the first process simulation system Flexible Flowsheet successfully developed by Kellogg. To date, the process simulation system has undergone four generations of development, from the initial simulation object mainly for light hydrocarbon processing to gradually developing a simulation object for a gas−liquid two-phase process and a gas−liquid−solid three-phase process. In the 1990s, simulation integrated steady-state and dynamic technologies, and it was widely used in the design, research, and production departments. Typical commercial process simulation software include Aspen plus, PRO/II, ChemCAD, Petro-Sim, and VMG-Sim.[2−6]

At present, chemical process simulation algorithms are mainly divided into two categories: sequential modular method (SM) and equation-oriented method (EO).[7] The sequential module method is currently widely used, but it has certain limitations. When the iteration times of the model calculation are high or the heat exchange process involved is complex, the model calculation is time-consuming and difficult to converge. Unlike the sequential module method, the EO method combines all of the equations for the process to form a nonlinear equation set and solves the variables involved simultaneously, which is more efficient and time-saving.[8,9] The difference between the two methods is shown in Figure 1.

Real-time optimization (RTO) is a technology that optimizes the operating conditions of the process in real time and downloads it to the control layer for automatic execution.[10] The RTO system of the refinery, which is generally based on a strict mechanism model and aims at maximizing economic benefits with scheduling indicators, equipment capacity, product quality, energy consumption, and other requirements as constraints, can achieve hour-level optimization of operation parameters and corresponding automatic execution.[11,12] At present, many petrochemical companies have begun to carry out RTO transformation and implementation of the main processing units in refineries, and the top-level architecture of an intelligent refinery is shown in Figure 2.[13−19] On the basis of these models, many other
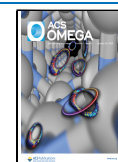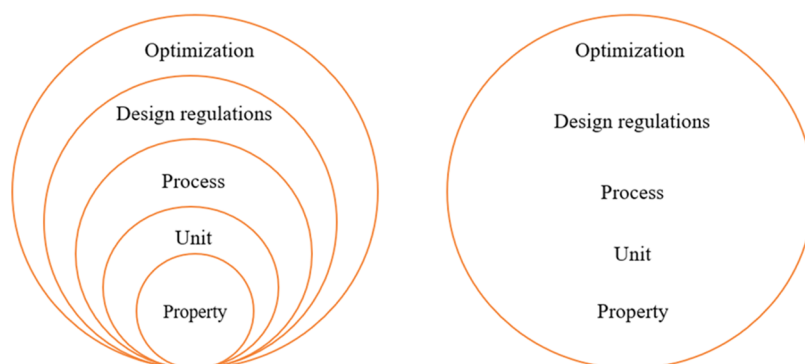
Figure 1. Sequential module method (left) and equation-oriented method (right).
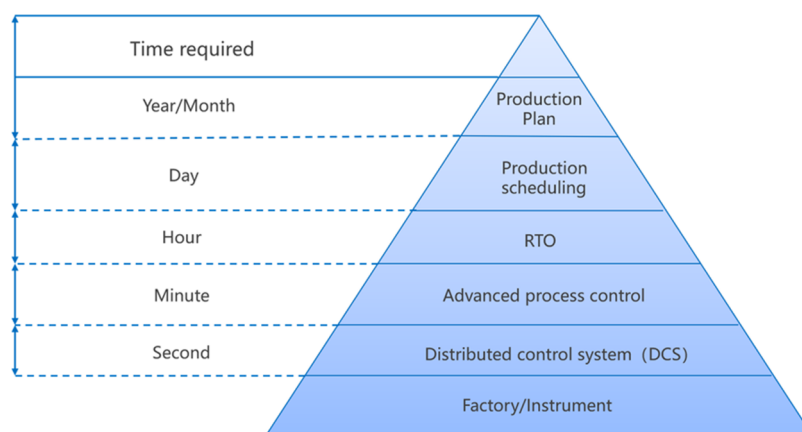

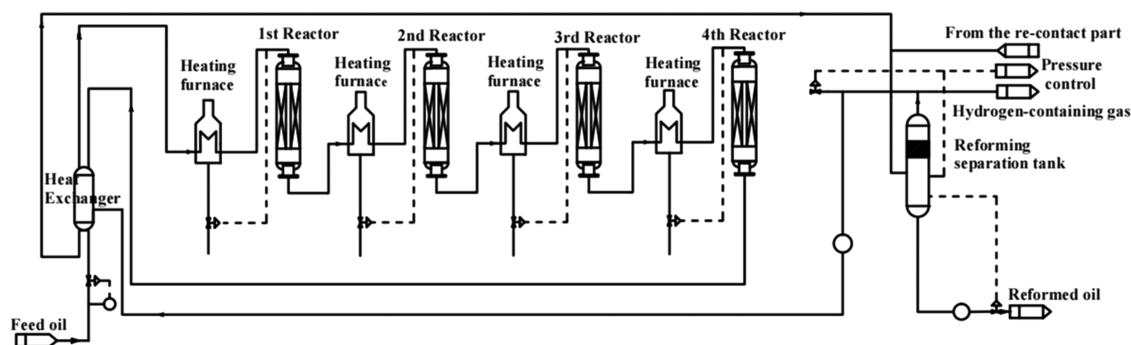**Figure 2.** Intelligent refinery architecture design.

Figure 3. Schematic diagram of the reaction-regeneration section of the countercurrent continuous reforming process.

researchers have used RTO in combination with other techniques for modeling and simulation.[20−23]

Catalytic reforming is one of the important secondary processing technologies in refining and petrochemical enterprises. It uses naphtha as a raw material to produce aromatic hydrocarbons and high-octane-number gasoline as well as the byproduct hydrogen.[24] In common chemical simulation software from Aspen Plus, KBC, and Schneider, the traditional cocurrent continuous reforming can be simulated, but the countercurrent continuous reforming process cannot be simulated because of its unique technological process. In the countercurrent continuous reforming process, the flow direction of the catalyst between each reactor is different from that of the cocurrent reforming, and the coke generation and deactivation of the catalyst in each reactor have an interaction with the reforming reaction depth. A more

reasonable solution to its simulation and optimization is to apply the equation-oriented method (EO) to perform the modeling and carry out simulation calculation of the entire process.

Sequential quadratic programming (SQP) and rSQP methods are the main optimization algorithms for the model built by the equation-oriented method currently. The equations that these algorithms can solve should be all algebraic equations, so the orthogonal configuration method or the finite element orthogonal configuration method is selected to discretize the differential equations such as the kinetic equations.[25] After establishing the whole process model with the EO method, it is necessary to calibrate the model. The main strategy of model calibration is to calibrate the kinetic parameters to make the calculated values more consistent with the actual values. After calibration, the operating conditions of
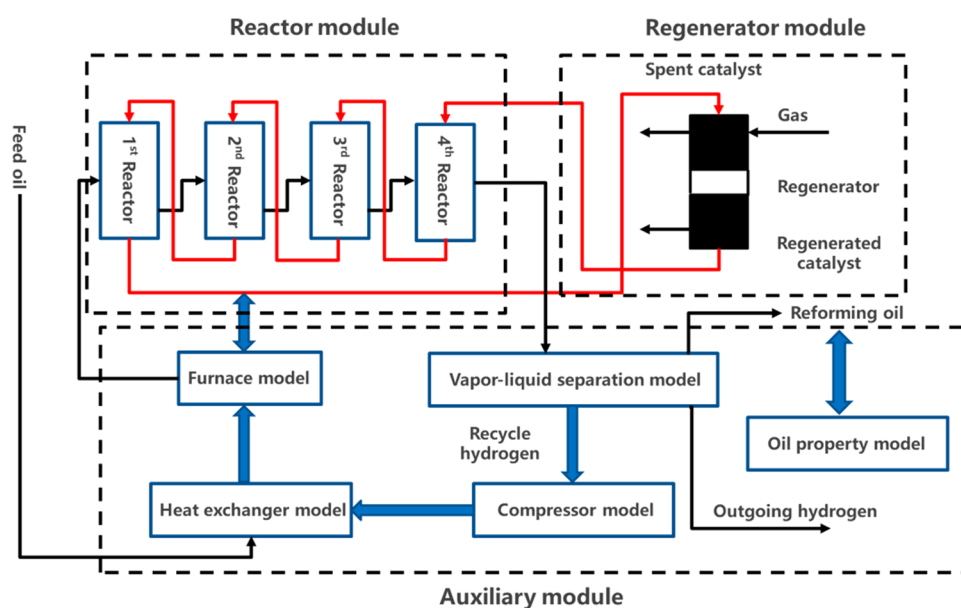
Figure 4. Overall architecture of the RTO model for countercurrent continuous reforming.

the countercurrent continuous reforming process can be optimized for specific raw materials to achieve maximum profit or other objectives.

2. OVERALL FRAMEWORK OF THE MODEL

2.1. Countercurrent Continuous Reforming Process. As shown in Figure 3, there are four reactors, a regenerator, a compressor, a heat exchanger, four heating furnaces, a reforming separation tank, and a hydrogen purification system in the reaction-regeneration section of the countercurrent continuous reforming process. Recycled hydrogen from the high-pressure separator tank is pressurized by a recycle hydrogen compressor and mixed with the reforming feedstock from the pretreatment section as the reforming feed. The feed exchanges heat with the products in a heat exchanger and then enters each reforming reactor in turn. Before entering each reactor, the material needs to be heated through a heating furnace in the front of the reactor to reach a specific reaction temperature. The high-temperature oil and gas from the fourth reactor exchange heat with the reforming feed, then are cooled by an air cooler, and finally enter the vapor−liquid separation tank. Part of the separated hydrogen-containing gas and the sealed and elevated hydrogen are used as recycled hydrogen. The other part is purified by the hydrogen purification system and sent as a byproduct out of the reforming process.[26]

During the reforming reaction, the catalyst and the reactant flow countercurrently, that is, the regenerated catalyst flows through the fourth reactor, the third reactor, the second reactor, and the first reactor and then returns to the regenerator for regeneration.[27,28] The catalysts with the highest activity in the third and fourth reactors are used to catalyze the difficult reactions such as alkane dehydrocyclization of paraffins, and the catalysts with a lower activity in the first and second reactors are used for easy reactions such as dehydroaromatization of naphthene. In short, matching the catalyst activity to the reaction difficulty is a significant advantage of the countercurrent continuous reforming process.

2.2. RTO Overall Structure. Countercurrent continuous reforming is a large-scale industrial process. In addition to modeling each of the units involved in the process mentioned

above, it is essential to establish the connection between each unit. The connection between the reactor module and the regenerator module is given by the equation associated with the coke deposition of the catalyst. The coke deposition at the first reactor outlet is the same as the coke deposition at the regenerator inlet, and the coke deposition at the regenerator outlet is same as the coke deposition at the fourth reactor inlet. The auxiliary module uses temperature as the connection between models that the compressor outlet temperature is the same as the inlet temperature of the heat exchanger, and the heat exchanger outlet temperature is the same as the inlet temperature of the heating furnace for the first reactor. The connections between each module are shown in Figure 4.

After connecting the modules together, the reaction-regeneration section of the process can be modeled by the EO method. The SQP method is adopted for solving the EO model as it can meet the requirements of the RTO without any further input of cumbersome entry conditions for each unit. Meanwhile, using the established oil property model, it is possible to estimate the physical properties of the reformed oil such as octane number, vapor pressure, end boiling point, distillation range, and density.

3. MODULE DETAILS

3.1. Reactor Module. Radial reactors are used to lower the pressure drop in countercurrent continuous reforming; its structure is shown in Figure 5. The 45-lump kinetic steady-state model developed by Jiang et al. of our team was used to simulate the reforming reaction.[29] Under normal reforming reaction operating conditions, the variation of concentration and temperature mainly happens in the radial direction, and there is little variation in the axial direction. To meet the requirements of real-time optimization, the reactor model is simplified to a one-dimensional radial model since the rate of coke deposition on the catalyst is relatively slow within the hydrogen environment and the two-dimensional model of the reactor will distinctly increase the burden of simulation calculation.[27,30] When establishing the EO model of the reaction module, it is necessary to simulate each radial reactor and determine the connections between the reactors.[31]
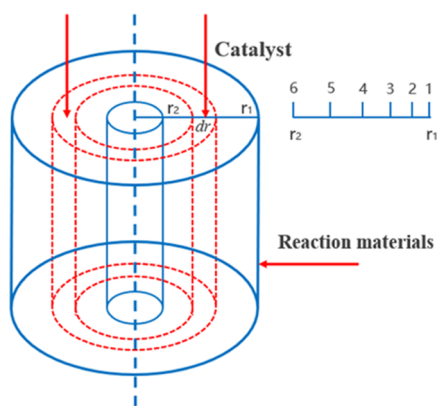
Figure 5. Diagram of the reactor structure.

The catalyst flows axially in each reactor by gravity, while the reactants flow radially in the radius direction. Between reactors for countercurrent catalytic reforming, the material flows in the direction opposite to that of the catalyst. In each reactor, material balance, momentum balance, and heat balance need to be taken into account, as the reactor is simplified to be an adiabatic system without heat losses.

(1) Material balance: It is assumed that the temperature, pressure, and molar flow rate of each component are uniformly distributed in the specific radial position of each reactor. The change in the molar flow rate with position is shown in eq 1.

$$dF(j)/dr = 2\pi r L \rho_b \sum r(j) \tag{1}$$

(2) Momentum balance: Ignoring the pressure drop of the manifold, the Eugen formula is used to calculate the pressure drop of the reactor.

$$dP/dr \cdot g = 150 \cdot \frac{1 - \varepsilon^2}{\varepsilon^3} \cdot \frac{\mu U}{\Phi d_p{}^2} + 1.75 \cdot \frac{1 - \varepsilon}{\varepsilon^3} \cdot \frac{\rho_f U^2}{\Phi d_p} \tag{2}$$

(3) Heat balance: The total heat of reaction and specific heat are obtained by calculating the related thermodynamic properties.

$$dT/dr = \frac{2\pi L \rho_b \sum r(j) H(j)}{\sum C_p(i) F(i)} \tag{3}$$

The effect of the catalytic deactivation reaction rate on the reaction is considered, and coke deposition in the reforming reaction is mainly generated by the dehydrogenation of alkanes and the condensation of aromatics and cycloalkanes.
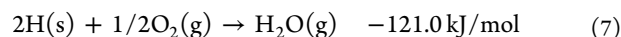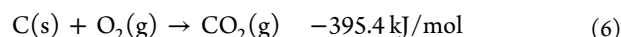
$$r_{coke} = \exp\left(k_{0,coke,N} - \frac{E_N}{RT}\right)\frac{P_N P_A}{P_H^2} + \exp\left(k_{0,coke,P} - \frac{E_P}{RT}\right)\frac{P_P}{P_H} \tag{4}$$

In the orthogonal collocation method, the Lagrange interpolation polynomial is used as the trial function of the approximation function, and the root of the Legendre polynomial is used as the collocation point. As the internal residual $R(\tau)$ is zero at the collocation point or the boundary point, the differential equations and boundary conditions are transformed into algebraic equations with parameters and then solved by the SQP algorithm.

$$R(\tau) = \sum_{i=0}^{K} Z_i \delta_i - f(x, Z_{K+1}(\tau)) \tag{5}$$

3.2. Regenerator Module. The regenerator of the catalytic reforming process is actually a radial reactor. The catalyst enters from the upper part, slides down along the axial direction gradually, and leaves the regenerator after oxidized combustion to remove the coke deposition on the catalyst; gas flows along the radial direction, and the oxygen in the gas reacts with the coke depositions to form carbon dioxide and water vapor. The regenerator model used in the process model is the countercurrent reforming regenerator steady-state model developed by Jiang Shubao et al. from our team.[32]

Coke is made up of carbon and hydrogen elements. Although the high ratio of carbon to hydrogen in coke can be analyzed and coke can be represented with the specific molecular formula corresponding to the ratio, the ratio will change as the coke reacts with oxygen because the hydrogen in coke is burned off at a higher rate than the carbon in coke. Thus, the reactions that take place in the regenerator can be described with two equations in the model.[33]

$$C(s) + O_2(g) \rightarrow CO_2(g) \quad -395.4\,kJ/mol \tag{6}$$

$$2H(s) + 1/2O_2(g) \rightarrow H_2O(g) \quad -121.0\,kJ/mol \tag{7}$$

Since catalyst regeneration is an exothermic process, both axial and radial heat balance are required, and it is necessary to establish a two-dimensional model to describe the regenerator. The regenerator is divided into several sections for simulation, and the axial position z and the radial position x of configuration points in each section are transformed into dimensionless numbers between 0 and 1. Material balance, momentum balance, and heat balance also need to be taken into account.

(1) Material balance

$$\frac{\partial C_c}{\partial z} = -\frac{(-r_C) \cdot \rho_b \cdot S \cdot L}{F_S} \tag{8}$$

$$\frac{\partial H_H}{\partial z} = -\frac{(-r_H) \cdot \rho_b \cdot S \cdot L}{F_S} \tag{9}$$

$$\frac{\partial F_{O_2}}{\partial x} = -(-r_{O_2}) \cdot \rho_b \cdot 2\pi L \times (r_0 - (r_0 - r_4)x) \times (r_0 - r_4) \tag{10}$$

$$\frac{\partial F_{CO_2}}{\partial x} = -(-r_{CO_2}) \cdot \rho_b \cdot 2\pi L \times (r_0 - (r_0 - r_4)x) \times (r_0 - r_4) \tag{11}$$

$$\frac{\partial F_{H_2O}}{\partial x} = -(-r_{H_2O}) \cdot \rho_b \cdot 2\pi L \times (r_0 - (r_0 - r_4)x) \times (r_0 - r_4) \tag{12}$$

(2) Heat balance

$$\frac{G_S C_{Ps}}{L} \cdot \frac{dT}{dz} + \frac{G_g \cdot C_{Pg}}{(r_0 - r_4)} \cdot \frac{dT}{dx}$$
$$= \rho_b((-\Delta H_c) \cdot (-r_C) + (-\Delta H_H) \cdot (-r_H)) \tag{13}$$

(3) Momentum balance

$$\frac{1}{-(r_0 - r_4)} \cdot \frac{dP}{dx} g = 150 \cdot \frac{1 - \varepsilon^2}{\varepsilon^3} \cdot \frac{\mu U}{d_p^2} + 1.75 \cdot \frac{1 - \varepsilon}{\varepsilon^3} \cdot \frac{\rho_f U^2}{d_p} \tag{14}$$

At the configuration point, the expressions of the partial derivative value in the axial direction and the radial direction are established, and the equation constraint is established according to the principle of the orthogonal configuration method that the residual is zero. The form of residuals is shown in eqs 15 and 16.

Residuals in the radial direction

$$R_x(z, x) = \sum_{j=1}^{N+2} y(z_l, x_j)B_{jk} - f_x(z, x) \tag{15}$$

Residuals in the axial direction

$$R_z(z, x) = \sum_{i=1}^{N+2} D_{li}y(z_i, x_k) - f_z(z, x) \tag{16}$$

After discretizing differential equations to get a series of equality constraints, the SQP algorithm is also used to solve the model.

3.3. Vapor–Liquid Separation Model. After the reformed gas comes out of the final reactor, it passes through an air cooler and finally enters a high-pressure separation tank for vapor–liquid separation. The gas-phase output is a mixed gas rich in hydrogen. Figure 6 is a schematic diagram of the separation tank of the catalytic reforming process.
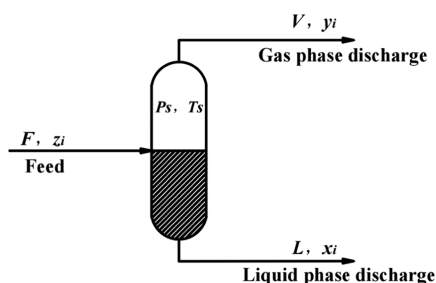
Figure 6. Diagram of the reforming separation tank.

Since vapor–liquid separation is generally carried out under the conditions of medium or low pressure (0.3–1.0 Mpa) and low temperature (30–60.6 °C), it is assumed that the gas phase is an ideal state and the liquid phase is also an ideal liquid. According to the principle of material balance and multicomponent vapor–liquid equilibrium, the steady-state model of the separation system can be expressed by the following equations

(1) Material balance

$$F = L_F + V_F \tag{17}$$

$$Fz_{Fi} = L_F x_{Fi} + V_F y_{Fi} \tag{18}$$

(2) Normalized equation

$$\sum_{i=1}^{44} z_{Fi} = 1 \tag{19}$$

$$\sum_{i=1}^{44} x_{Fi} = 1 \tag{20}$$

$$\sum_{i=1}^{44} y_{Fi} = 1 \tag{21}$$

(3) Phase equilibrium of the mixture components

$$\frac{y_{Fi}}{x_{Fi}} = \frac{p_{Fi}^0}{P_s} = k_{Fi} \tag{22}$$

The Antoine formula is used to calculate the saturated vapor pressure of each component P_{Fi}^0 for eq 22, since the temperature and pressure of the reforming separation tank are not very high.

$$p_{Fi}^0 = 10^{[(A-B/(T+C)]} \tag{23}$$

The coefficients A, B, and C in the above formula are shown in Table S1.

According to eqs 24, 44 constraint equations can be obtained. The SQP algorithm is also used to solve the constraint equations.

$$y_{Fi} - k_{Fi}\cdot x_{Fi} = 0 \tag{24}$$

3.4. Heating Furnace Model. In the continuous reforming process, the temperature drop of oil and gas at the outlet of the first reactor can be up to about 100 °C, and the temperature drops of oil and gas at the outlets of the second, third, and fourth reactors can also reach 75, 58, and 45 °C, respectively. Therefore, before the entrance of each reactor, there is a heating furnace to increase the temperature of the reactants to ensure the required reaction temperature for reforming.[34]

In process simulation, it is necessary to calculate the accurate heat efficiency of the furnace so as to obtain the heating load, which should be less than its upper limit in the optimization calculation. The heat efficiency is equal to the percentage of effective heat divided by the supplied heat.

The heating furnace is equipped with a convection section near the flue gas outlet, and heat transfer is carried out by radiation and convection; the structure of the heating furnace is shown in Figure 7. According to the Q/Y50-2002 energy
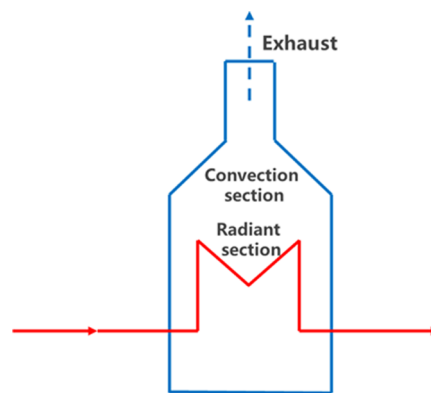
Figure 7. Diagram of the heating furnace.

conservation monitoring method of the petrochemical process heating furnace of China National Petroleum Corporation,[35] the percentage of heat loss to the total heat can be calculated by the counterbalancing method first when calculating the thermal efficiency.

$$\eta_H = 100 - q_1 - q_2 - q_3 \tag{25}$$

$$q_1 = [(8.3 \times 10^{-3} + 0.031\alpha) \cdot (tg + 1.35 \times 10^{-4} tg^2) - 1.1] \tag{26}$$

$$q_2 = (4.043\alpha - 0.252) \cdot HCO \cdot 10^{-4} \tag{27}$$

α is the overheated air coefficient.

$$\alpha = (21 - 0.0627 \times HO_2)/(21 - HO_2) \tag{28}$$

Surface heat loss can be obtained through the heat provided by the fuel minus the sum of heat for the heating process medium, the heat used to produce steam, and the heat loss with the exhaust gas.

The total heat provided by the fuel is equal to the calorific value of the fuel gas multiplied by its flow rate.

$$Q_{total} = F_{fg} \times Q_{sf} \tag{29}$$

The heat consumed for the heating process medium is calculated by the molar flow rate of the material as well as the inlet and outlet temperatures of each heating furnace.

$$Q_H = F \times \int_{T_{Fout}}^{T_{Fin}} C_p(T)\, dT \tag{30}$$

The amount of heat needed to produce steam is calculated from the steam system heat. By referring to HSC software, the standard enthalpy of feed water and generated steam is obtained; then, the heating load of the steam is obtained by the flow rate of water.

$$Q_w = H_w^\theta \times L_w - H_G^\theta \times L_G \tag{31}$$

Therefore, the surface heat loss can be calculated by eq 32.

$$Q_{sur} = Q_{total} - Q_H - Q_w - Q_{total}(q_1 + q_2) \tag{32}$$

The ratio of the surface heat loss to the total heat provided is denoted q_3. The effective heating load of the heating furnace is equal to the heat provided by the fuel multiplied by the heat efficiency η_H.

$$Q_{eff} = Q_{total} * \eta_H \tag{33}$$

When applying the above formula to calculate the heating furnace efficiency, the required known variables and calculated variables are as shown in Table S2.

3.5. Compressor Model. In the countercurrent continuous reforming process, the recycled hydrogen from the reforming separation system enters the recycle hydrogen compressor, which is a key power equipment of the reforming process.[36] Under the effect of the compressor, the recycled hydrogen is pressurized to a specified pressure and enters the heat exchanger to increase the temperature. To accurately calculate the steam consumption of the compressor and the outlet temperature of the recycled hydrogen, the compressor steady-state model needs to be established.

The process that occurs in the recycle hydrogen compressor can be regarded as a polytropic process, in which the adiabatic index of each substance can be found through the handbook of thermodynamic data, and the total adiabatic index of recycled hydrogen is calculated by eq 34.

$$\frac{1}{k_H - 1} = \sum \frac{y_{He}}{k_{He} - 1} \tag{34}$$

According to the actual inlet flow rate, the corresponding polytropic efficiency and the compression ratio can be obtained when the inlet and outlet pressures are known. The polytropic index m_h is calculated from the corresponding polytropic efficiency and the adiabatic index.

$$m_h = 1/[1 - 1/(\eta_p k_H/(k_H - 1))] \tag{35}$$

The outlet temperature of the recycled hydrogen in the compressor is calculated with the polytropic index and the compression ratio.

$$T_{Eout} = T_{Ein} \varepsilon_c^{[(m_h - 1)/m_h]} \tag{36}$$

After calculating the outlet temperature, the polytropic index can be calibrated according to the actual outlet temperature. With the calibrated polytropic index, the theoretical power of the compressor can be calculated using eq 39.

$$N = \frac{16.67 P_1 V_1 \frac{m_h}{m_h - 1} [\left(\frac{P_2}{P_1}\right)^{m_h - 1/m_h} - 1]}{\eta_p} \tag{37}$$

The shaft power is equal to the theoretical power divided by the mechanical efficiency and the transmission efficiency.

$$N_s = N/\eta_g/\eta_e \tag{38}$$

When calculating the value of steam consumption, it is necessary to calculate its enthalpy difference before and after compression.

$$G_E = 3600 N_S/\Delta H_s/\eta_i/\eta_g \tag{39}$$

When applying the above formula to calculate the steam consumption of the compressor, the required known variables and calculated variables are shown in Table S3.

3.6. Heat Exchanger Model. The temperature of the hydrogen from the compressor is about 80 °C, and the temperature of the feed oil from the pretreatment distribution is about 110 °C, while the temperature of the oil and gas mixture at the inlet of the heating furnace is above 400 °C. To accurately calculate the reforming reaction heat and the heating load of the heating furnace, it is necessary to estimate the inlet temperature of the reforming feedstock stream into the first heating furnace.[37] This is the main reason for establishing the heat exchanger steady-state model.

The reforming process uses a plate heat exchanger. Because the main target of the estimation is the outlet temperature, it is assumed that this process is a countercurrent heat-transfer process without phase change. A model is established through the macroscopic energy balance equation and the total heat-transfer equation of the heat exchanger.

$$Q_{ex} = W_h(H_{h,1} - H_{h,2}) = W_c(H_{c,2} - H_{c,1}) = AS \cdot K_{gross} \cdot \Delta T_{LMTD} \tag{40}$$

$$\Delta T_{LMTD} = \frac{\Delta t_h - \Delta t_c}{\ln\left(\frac{\Delta t_h}{\Delta t_c}\right)} \tag{41}$$

Among them, the value of K_{gross} is obtained by fitting the actual heat exchanger outlet temperature. The error due to ignoring the phase transition and heat loss is calibrated by the estimation of the heat-transfer coefficient; the required known variables and calculated variables are shown in Table S4.

3.7. Oil Property Model.

3.7.1. Octane Number Estimation Model. The octane number is the most important quality indicator of motor gasoline, and the octane number of gasolines has a strong relationship with its composition.[38] The octane number of the mixed components is calculated by eq 42.

$$\text{RON} = k_{\text{RON}} \sum_{i=1}^{44} a_i L_{\text{F}i} \tag{42}$$

The octane number coefficients in eq 42 are shown in Table S5.[39]

The octane number calculated by the model is verified with actual analysis data, and the model fitting effect is shown in Figure 8.
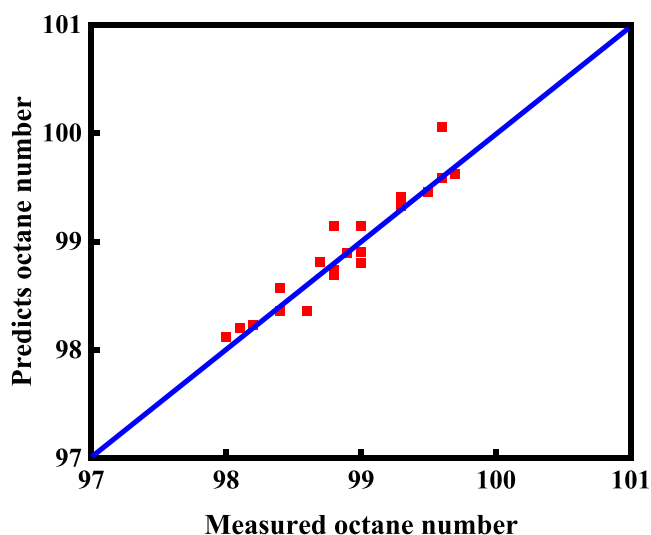

Figure 8. Fitting results of the octane number.

The comparison results show that the absolute error of model prediction is less than 1, which means that the accurate octane number can be obtained without adjusting the effective octane number of each component or changing the mathematical model due to the large difference in oil composition.

3.7.2. Vapor Pressure Estimation Model. Since the pressure is not too high, the gas and liquid phases can be treated as ideal gas and ideal liquid, respectively.

Saturated vapor pressure of the mixed fraction is calculated using eq 43.

$$P_{\text{total}} = \sum_{i=1}^{44} P_{\text{F}i}^0 L_{\text{F}i} \tag{43}$$

Calculation of saturated vapor pressure still adopts the Antoine formula. Comparing the calculated steam pressure with the actual analysis data, the fitting effect of the model is shown in Figure 9.

It can be concluded that the errors between the calculated vapor pressure and the actual value are mostly less than 1 kpa, which means that the estimation model can be used to calculate the vapor pressure.

3.7.3. End Boiling-Point Estimation Model. The temperature when the last drop of oil sample in the flask disappears is called the dry point or the end boiling point of the fraction.
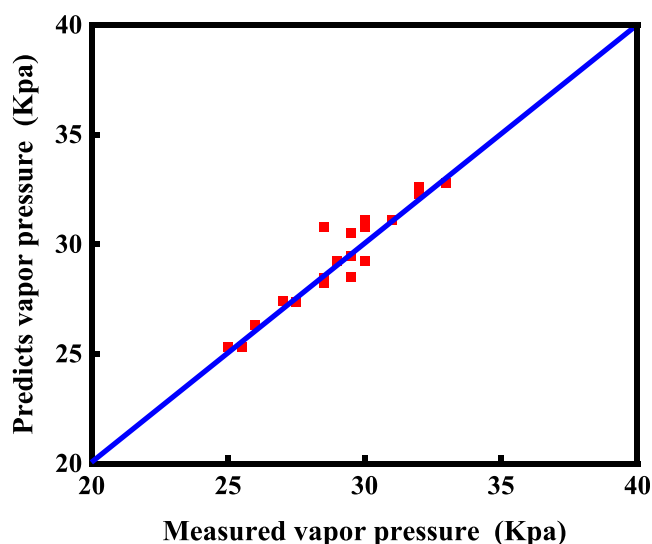
Figure 9. Fitting results of vapor pressure.

The end boiling point is generally only related to the content of the heaviest components in a fraction.

The end boiling point of the mixed components is calculated by eq 44.

$$\text{Ebp} = \sum_{i=1}^{5} k_{\text{Ebp}} L_{\text{F}i} + B_{\text{bp}} \tag{44}$$

The coefficients for estimation are shown in Table S6 as the concentrations of C_{11} and C_{12} alkanes are zero.

The model fitting effect is shown in Figure 10.
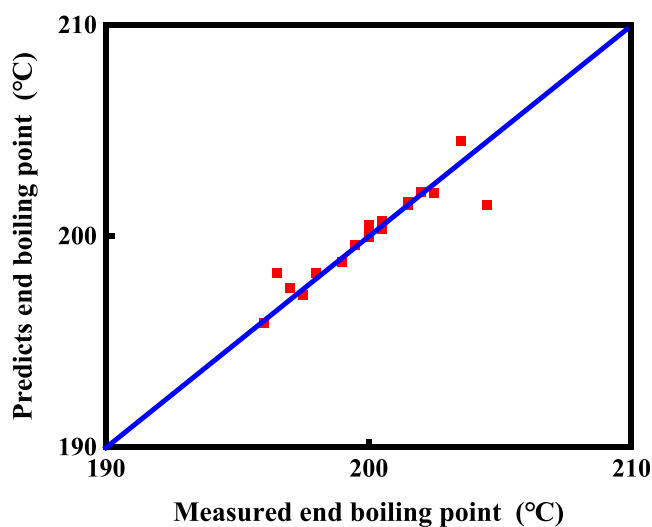
Figure 10. Fitting results of the end boiling point.

It can be concluded that the relative errors between the calculated end boiling point and the actual value are less than 1%.

3.7.4. Density Estimation Model. Density of the mixture is calculated by eq 45.

$$\rho_{\text{total}} = \sum_{i=1}^{44} k_\rho L_{\text{F}i} / 100 - \Delta_\rho \tag{45}$$

The value of the calculated correction coefficient Δ_ρ is 8 kg/m^3, and the density coefficients in eq 45 are shown in Table S7.

The calculated reforming oil density is verified with the actual analysis data, and the model fitting effect is shown in Figure 11.

Figure 11. Density fitting results.

It can be concluded that the relative errors between the calculated density and the measured density are mostly less than 1%, which means that the density estimation model can be used to determine the density of reforming oil.
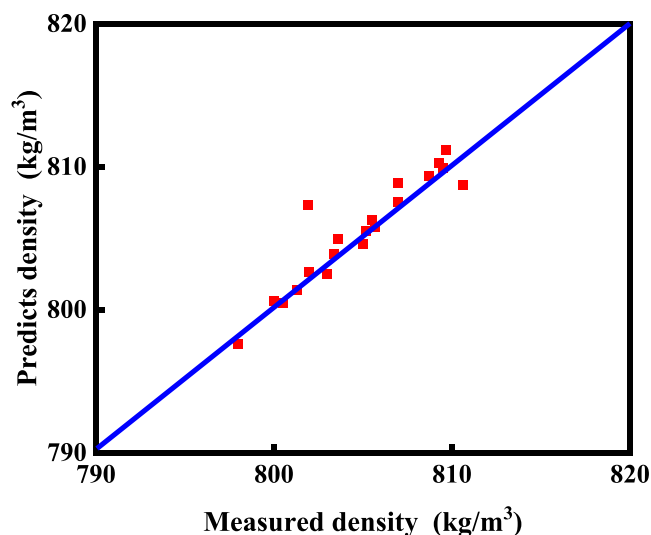
3.7.5. Distillation Range Estimation Model. The distillation range measurement method commonly used in the actual industry is ASTM D86, but the distillation curve based on the boiling point and percentage of individual components is closer to the simulated distillation curve. The simulated distillation based on temperature programming of gas chromatography requires less analysis time than real boiling-point distillation and has more theoretical plates.

First, the simulated distillation data is converted to real boiling-point distillation data.[40]

$$TBP(5 \text{ wt }\%) = TBP(50 \text{ wt }\%) - VV_5 - VV_6 - VV_7 \tag{46}$$

$$TBP(10 \text{ wt }\%) = TBP(50 \text{ wt }\%) - VV_5 - VV_6 \tag{47}$$

$$TBP(30 \text{ wt }\%) = TBP(50 \text{ wt }\%) - VV_5 \tag{48}$$

$$TBP(50 \text{ wt }\%) = SD(50 \text{ wt }\%) \tag{49}$$

$$TBP(70 \text{ wt }\%) = TBP(50 \text{ wt }\%) + VV_4 \tag{50}$$

$$TBP(90 \text{ wt }\%) = TBP(50 \text{ wt }\%) + VV_4 + VV_3 \tag{51}$$

$$TBP(95 \text{ wt }\%) = TBP(50 \text{ wt }\%) + VV_4 + VV_3 + VV_2 \tag{52}$$

$$TBP(100 \text{ wt }\%) = TBP(50 \text{ wt }\%) + VV_4 + VV_3 + VV_2 + VV_1 \tag{53}$$

In the above formula, VV is calculated from eq 54.

$$VV_{Di} = D \cdot (WW_{Di})^E \tag{54}$$

D and *E* are coefficients as shown in Table S8.

Second, the real boiling-point distillation data is converted to ASTM D86 distillation data.

$$ASTM_{Di} = \frac{\left(\frac{1.8}{F} \cdot TBP(\text{wt }\%)\right)^{1/G}}{1.8} \tag{55}$$

F and *G* are coefficients, as shown in Table S9.

The calculated data is compared with the actual distillation range data, and the results are shown in Table 1.

The relative errors of the calculated and actual distillate data are small, which means that the distillation range estimation model can be applied in this process.

4. MODEL CALIBRATION

In the actual industry, the performances of the catalyst and the operating state change slightly with time, so it is necessary to calibrate the reactor model to reflect the current catalyst performance and operating state of the process. During the calibration, it is not necessary to calibrate every kinetic parameter but to calibrate the pre-exponential factors of various reforming reactions. For each type of reaction, the pre-exponential factors are multiplied by a coefficient where the initial value of the coefficient is set to 1 and its range is between 0.9 and 1.1 for optimization with the SQP algorithm. The objective function of optimization is set to be the sum of squares of the differences between the calculated and actual values, including the temperature, catalyst coke deposition, and molar flow of each component, and the equality constraints for the material balance, heat balance, and momentum balance are the same as the reactor module of Section 3.1.

$$f_{ca} = \sum_{i=1}^{44} Y_{F,i}(F_{i,\text{real}} - F_{i,\text{cal}})^2 + Y_T$$
$$\sum_{q=1}^{4} (T_{q,\text{out,real}} - T_{q,\text{out,cal}})^2$$
$$+ Y_w(w_{\text{coke,1,out,real}} - w_{\text{coke,1,out,cal}})^2 \tag{56}$$

The first to third sets of data in Table S10−S14 were used for calibration, and the optimized calibration coefficients are as shown in Table 2. In general, it takes 15 min to calculate the calibrated model coefficients on MATLAB (CPU = 2.20

Table 1. Results of Distillation Range Estimation

	actual data (°C)			model data (°C)			
number	ASTM (10 wt %)	ASTM (50 wt %)	ASTM (90 wt %)	ASTM (10 wt %)	ASTM (50 wt %)	ASTM (90 wt %)	relative error (%)
1	83.5	127	170.5	85.47	126.85	166.97	1.49
2	85	123.5	164.5	85.41	123.05	165.68	0.52
3	85.5	123.5	164.5	84.50	120.79	166	1.42

Table 2. Calibration Coefficients

reaction	calibration coefficient
dehydrogenation, $N \rightleftharpoons A$	1.005
dehydrogenation, $P \rightleftharpoons O$	0.995
dehydrocyclization, $P \rightleftharpoons N$	1.000
isomerization, $iP \rightleftharpoons nP$	1.004
isomerization, $5N6 \rightleftharpoons 6N6$	1.100
transalkylation, $2A \rightleftharpoons A + A$	0.947
hydrocracking, $nP \rightarrow P$	1.005
hydrocracking, $iP \rightarrow P$	0.999
hydrodealkylation, $A \rightarrow A + P$	1.003
adductive reaction, $P + O \rightarrow P$	1.068
adductive reaction, $A + O \rightarrow A$	1.100
$A + N \rightarrow Coke$	0.922
$P \rightarrow Coke$	0.998

GHz). The speed of convergence depends on the initial settings and the accuracy requirement.

The calculated temperature before and after calibration as well as the actual temperature are compared, as shown in Table 3.

Table 3. Error of Temperature Before and After Calibration

number of data sets	before calibration (K)	after calibration (K)	actual value (K)	absolute error1	absolute error2
1	688.14	684.70	683.05	0.75	0.24
	711.41	710.29	708.07	0.47	0.31
	725.48	725.58	726.40	0.13	0.11
	729.01	730.20	730.23	0.17	0.00
2	685.86	682.49	683.95	0.28	0.21
	709.46	708.33	708.42	0.15	0.01
	724.17	724.23	726.97	0.39	0.38
	728.79	729.97	730.84	0.28	0.12
3	683.03	679.65	684.45	0.21	0.70
	707.43	706.28	708.17	0.10	0.27
	722.46	722.51	725.86	0.47	0.46
	727.63	728.78	728.64	0.14	0.02

It can be concluded that the absolute error between the actual temperature and the calibration temperature is greatly reduced, and the average absolute error is reduced by 19.26%.

The calculated coke deposition before and after calibration as well as the actual coke deposition are compared as shown in Table 4.

Table 4. Error of Coke Deposition Before and After Calibration

number	before calibration (%)	after calibration (%)	actual value (%)	asolute error1 (%)	absolute error2 (%)
1	0.0257	0.0268	0.0293	0.0036	0.0025
2	0.0280	0.0293	0.0287	0.0007	0.0005
3	0.0227	0.0237	0.0245	0.0018	0.0008

It can be concluded that the absolute error between the actual coke deposition and the calibration coke deposition is greatly reduced, and the average absolute error is reduced by 37.07%.

The comparison of material molar flow before and after calibration is shown in Figure 12.

Before model calibration, the prediction absolute errors of the total molar flow rate of the three sets of data are 16.65, 27.03, and 37.35 kmol/h, respectively; after calibration, the prediction absolute errors are 1.82, 12.66, and 23.29 kmol/h, respectively. The average absolute errors of each component before calibration of the three sets of data are 1.19, 1.36, and 1.44 kmol/h, respectively; the average absolute errors of each component after calibration are 0.69, 0.96, and 1.0 kmol/h, respectively. It can be concluded that the calibration effect is very effective, which can achieve the purpose of matching the calculated value and the actual value more closely.

5. PROCESS SIMULATION

Based on the simulation of the calibrated model, the temperature profile and molar flow changes of the various fractions in the process can be obtained. The fourth set of data in Tables S10−S14 and the regenerator data in Table S15 were chosen as the feed composition and operation conditions for simulation. The SQP method has the advantages of high accuracy and fast convergence. In general, it takes only 25 s to simulate the reaction-regeneration section of the countercurrent continuous reforming process on MATLAB (CPU = 2.20 GHz).

In the entire process model, the coke deposition of the catalyst is an important parameter as the catalyst circulates between the reactors and the regenerator. At the same time, using the EO method to simulate the process is also suitable for other processes, such as the cocurrent continuous reforming process. The trend of coke deposition of the catalyst in each module of the countercurrent reforming process and the cocurrent reforming process is shown in Figure 13.

For the countercurrent reforming process, the increase of coke deposition on the catalyst is the largest in the fourth reactor, and the increase is relatively slow in the first, second, and third reactors. This is because the regenerated catalyst enters the fourth reactor first in the countercurrent continuous reforming, the condensation of aromatics will be intensified due to the high activity of the catalyst and the high content of aromatic hydrocarbons and olefins in the fourth reactor.

As a comparison, the cocurrent reforming process was also simulated. The flow direction of the catalyst was changed to be consistent with the flow direction of the material, without changing the amount of catalyst loading in each reactor, and the coke deposition of the catalyst under cocurrent catalytic reforming was obtained. In the cocurrent reforming process, the catalysts in the first and second reactors have a high activity because of less coke deposition of the catalysts than that of the countercurrent reforming process, and the main reforming reactions are easy to happen, such as alkane dehydrogenation cyclization and cycloalkane dehydrogenation aromatization. In the third and fourth reactors, due to the decrease in catalyst activity and the increased coke deposition, the coke deposition of the catalyst at the outlet of the fourth reactor is more than that in the countercurrent process. However, in the actual cocurrent reforming process, the first reactor has the smallest catalyst loading amount and the fourth reactor has the largest catalyst loading amount, which will lead to a larger difference in catalyst coke deposition among the four reactors. As a result, the countercurrent continuous reforming process can make the catalyst activity and reaction difficulty more suitable.

In the regenerator module, the combustion reaction mainly happens in the first stage of the regenerator, and the remaining coke deposition on the catalyst is removed in the second stage
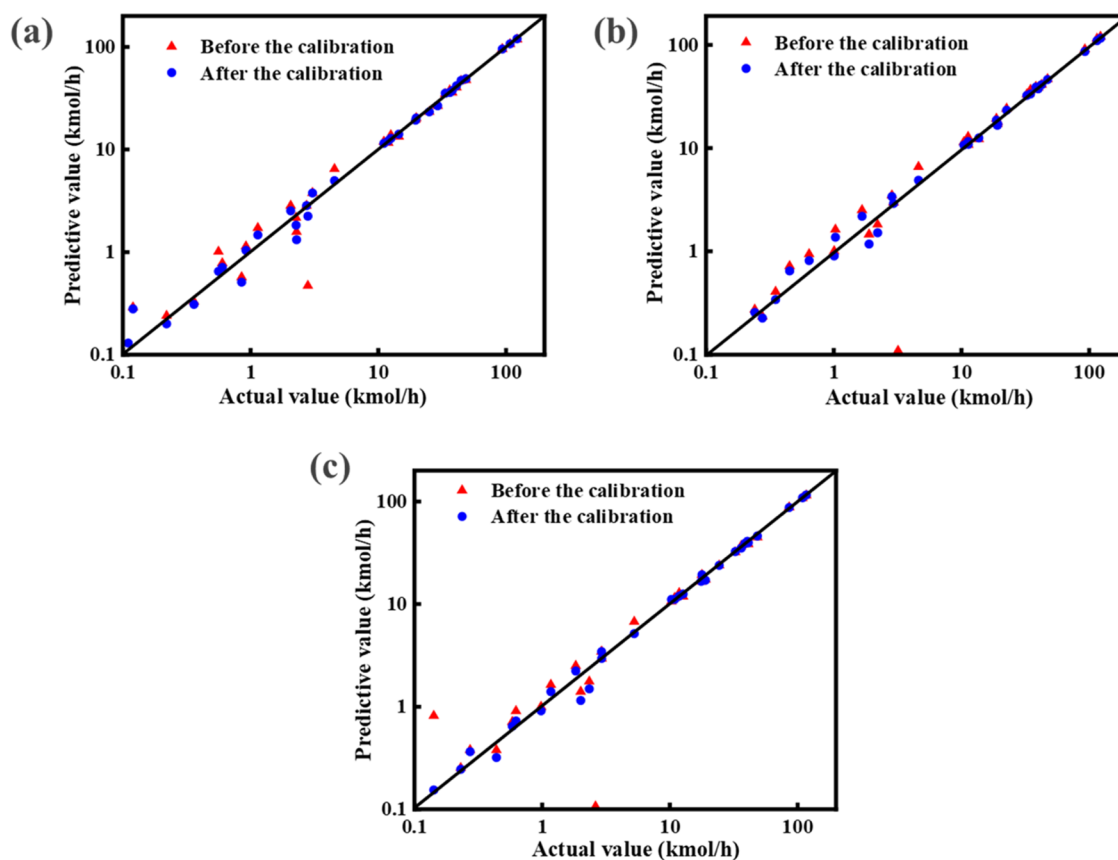
Figure 12. Comparison of material molar flow: (a) first set of data, (b) second set of data, and (c) third set of data before and after calibration.
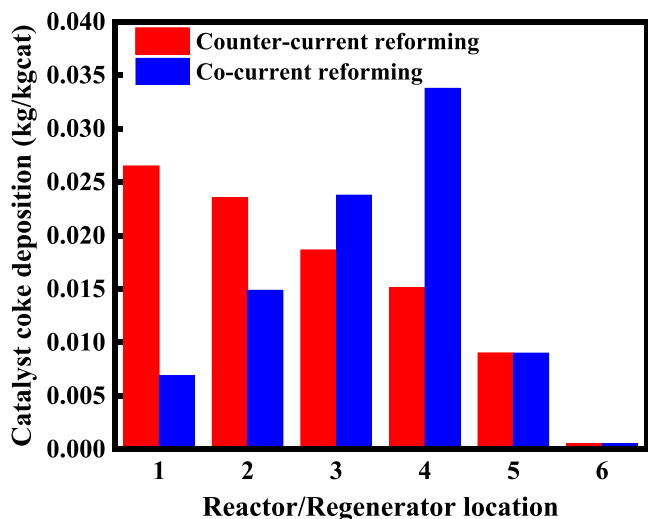
Figure 13. Trend of coke deposition in the process. Position: 1, first reactor outlet; 2, second reactor outlet; 3, third reactor outlet; 4, fourth reactor outlet; 5, first stage outlet of the regenerator; 7, second stage outlet of the regenerator.

trends of the recycled hydrogen and the feed oil are shown as Figure 14.
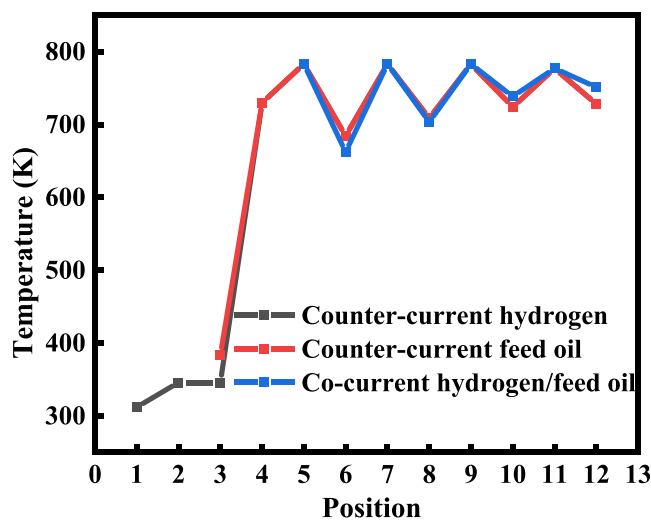
Figure 14. Temperature trends of hydrogen and feed oil.

Position: 1, compressor inlet; 2, compressor outlet; 3, heat exchanger inlet; 4, heat exchanger outlet; 5, first heating furnace outlet; 6, first reactor outlet; 7, second heating furnace outlet; 8, second reactor outlet; 9, third heating furnace outlet; 10, third reactor outlet; 11, fourth heating furnace outlet; 12, fourth reactor outlet.

As shown in Figure 14, the heating load of the heat exchanger is the largest in the entire reforming process. For

of the regenerator to assure full recovery of the catalyst activity. Due to the redundant capacity of the regenerator design, the coke deposition generated by either the countercurrent continuous reforming or the cocurrent continuous reforming can be completely burned.

During the countercurrent continuous reforming process and cocurrent continuous reforming process, the temperature

countercurrent continuous reforming, the temperature drop in the first reactor is 98.59 °C, and the temperature drops of the second, third, and fourth reactors are 74.31, 58.85, and 48.91 °C, respectively. For the cocurrent continuous reforming process, the temperature drop in the first reactor is 120.79 °C, and the temperature drops of the second, third, and fourth reactors are 74.59, 44.51, and 35.7 °C, respectively. The temperature difference between the reactors in countercurrent continuous reforming is larger than that in the countercurrent continuous reforming. In the actual cocurrent reforming process, the amount of catalyst loading in each reactor will be changed to make the temperature difference between the four reactors smaller, but this will lead to a lower efficiency of catalyst utilization.

The simulation results show that the countercurrent continuous reforming model can be established by the EO method, and the model can be easily modified for the simulation of cocurrent continuous reforming. The EO method is effective for the modeling of petrochemical processes with a complex reaction system.

6. PROCESS OPTIMIZATION

6.1. Optimized Strategy. For industrial processes, optimization mainly includes improving the selectivity or yield of the product and achieving the maximum economic benefits based on the raw material composition and market demand, in the premise of meeting the product indicators. Optimization can be categorized into offline optimization and online optimization.[41] The feature of online optimization is that the device can be kept in an optimal state for a long time so as to achieve deeper optimization. The general form of the mathematical model of the constrained nonlinear optimization problem (also called the nonlinear programming problem) can be shown by eqs 57 and 58.

$$\min J(\vec{x})$$

$$g_i(\vec{x}) \geq 0, \, i = 1, 2, \cdots, \tag{57}$$

$$h_j(\vec{x}) = 0, \, j = 1, 2, \cdots, \tag{58}$$

The SQP algorithm can also be used to solve the constrained nonlinear programming problem, and the optimal operating conditions can be selected to achieve energy saving and consumption reduction and increase the yield of reformed gasoline/aromatics to maximize the process profits.

For the continuous reforming process, an important purpose is to produce basic organic materials such as benzene, toluene, and xylene. In this case, the objective function of optimization is set as the yield of aromatics. Another important product of continuous reforming is the production of high-octane gasoline. In this case, the objective function of optimization is set as the yield of high-octane gasoline.

In actual operations of countercurrent reforming, the operating variables that can be changed are mainly the inlet temperature of the four reactors, the H/C molar ratio, as well as the inlet temperature and oxygen content of the regeneration gas. Constraints include the coke deposition on the catalyst of the first reactor outlet, coke deposition on the catalyst of the regenerator outlet, inlet oxygen content of gas for the regenerator, the amount of steam consumed by the compressor, and the heating load of heating furnaces.

For the production plan of aromatics, the objective function is aromatic yield, as in eq 59.

$$\min J(\vec{X}) = -f_1(\vec{X})_1$$
$$= -(W_{A6} + W_{A7} + W_{A8} + W_{A9} + W_{A10} + W_{A11}$$
$$+ W_{A12}) \tag{59}$$

For the production plan of gasoline, the objective function is the yield of high-octane gasoline, as in eq 60.

$$\min J(\vec{X}) = -f_1(\vec{X})_2$$
$$= -(W_{np4} + W_{np5} + W_{np6} + W_{np7} + W_{np8}$$
$$+ W_{np9} + W_{np10} + W_{np11} + W_{np12} + W_{ip4}$$
$$+ W_{ip5} + W_{ip6} + W_{ip7} + W_{ip8} + W_{ip9} + W_{ip10}$$
$$+ W_{ip11} + W_{ip12} + W_{O4} + W_{O5} + W_{O6} + W_{O7}$$
$$+ W_{O8} + W_{O9} + W_{O10} + W_{O11} + W_{5N6}$$
$$+ W_{6N6} + W_{N7} + W_{N8} + W_{N9} + W_{N10}$$
$$+ W_{N11} + W_{A6} + W_{A7} + W_{A8} + W_{A9} + W_{A10}$$
$$+ W_{A11} + W_{A12}) \tag{60}$$

Within the upper and lower limits of operating conditions, the inlet temperature of the reactor should not be too high because of the coke deposition limit, the inlet temperature should not be too low to ensure a certain conversion, and the upper limit of the H/C molar ratio should consider the upper limit of steam consumption of the compressor. The upper limit of the inlet gas temperature and the oxygen content of the regenerator is to ensure that the temperature of the hot spot in the regenerator is not too high. When the objective function is high-octane gasoline yield, the other restriction is that the octane number should not be less than 98. Specific values are shown in Table 5.

6.2. Optimization Results. Under Table 5 constraints, the optimized results of operating conditions are as shown in Table 6. In process optimization, it takes 5 minutes to calculate

Table 5. Upper and Lower Limits of Operating Conditions

restrictions	constraint value	
	lower limit	upper limit
1st reactor input temperature (K)	778.15	788.15
2nd reactor input temperature (K)	778.15	788.15
3rd reactor input temperature (K)	778.15	788.15
4th reactor input temperature (K)	771.15	781.15
H/C molar ratio (mol/mol)	2.0	2.3
regeneration gas inlet temperature (K)	/	735
regenerator oxygen content (%)	/	0.008
heating load (MW/h)	/	25
steam consumption (t/h)		10
reactor outlet catalyst coke deposition (kg/kgcat)	/	0.035
regenerator outlet catalyst coke deposition (kg/kgcat)	/	0.0005
aromatic yield (wt %)	/	
gasoline yield (wt %)	/	
octane number[a]		98

[a]The constraint is only when the objective function is the high-octane gasoline yield.

the values of the optimized operating conditions on MATLAB (CPU = 2.20 GHz).

Table 6. Optimization Results[a]

restrictions	operating status	optimization results	
		I	II
1st reactor input temperature (K)	783.15	787.82	779.97
2nd reactor input temperature (K)	783.15	785.34	778.15
3rd reactor input temperature (K)	783.15	786.57	778.18
4th reactor input temperature (K)	776.15	780.43	771.14
H/C molar ratio (mol/mol)	2.12	2.05	2.08
regeneration gas inlet temperature (K)	729.86	727.86	726.25
regenerator oxygen content (%)	0.06105	0.080	0.077
heating load (MW/h)	18.554	20.56	19.29
steam consumption (t/h)	9.4	9.7	9.3
reactor outlet catalyst coke deposition (kg/kgcat)	0.0247	0.0258	0.0224
regenerator outlet catalyst coke deposition (kg/kgcat)	0.000536	0.0005	0.0005
aromatic yield (wt %)	61.72	62.71	61.62
gasoline yield (wt %)	81.74	82.26	83.37
octane number	99.3	99.77	98.14

[a]Optimization results I correspond to eq 59, where the objective function is the optimization result of the aromatic hydrocarbon yield; optimization results II correspond to eq 60, where the objective function is the optimization result of the gasoline yield.

In some cases, it is favored to produce more C_7^+ aromatics, and the constraint setting of the operating conditions is the same as that of the production of aromatics, and the objective function is changed to eq 61.

$$\min J(\vec{X}) = -f_1(\vec{X})_3$$
$$= -(W_{A7} + W_{A8} + W_{A9} + W_{A10} + W_{A11} + W_{A12}) \tag{61}$$

Under such conditions, the optimization results are as shown in Table 7. The optimization time is similar to that required for aromatic yield optimization.

Under the existing operating conditions, the yield of aromatic hydrocarbons is increased by 0.99% when the objective function is the yield of aromatic hydrocarbons, and the yield of gasoline is increased by 1.63% when the objective function is the yield of gasoline with a high octane number. Taking the C_7^+ aromatic yield as the target, the yield increased by 0.74%, while the aromatic yield also increased by 0.94%. Thus, the economic profits of the improvement are considerable.

From the optimization results, the change in operating conditions to improve the aromatic yield is mainly the increase of the reactor inlet temperature. Corresponding to the reaction mechanism of aromatic generation, the increase in temperature is favorable to the alkane dehydrocyclization reaction and the cycloalkane dehydrogenation reaction, which can improve the yield of aromatics.

The limiting condition in gasoline yield optimization is mainly the octane number because a lot of the increase in gasoline yield consists of C_{10}^+ fractions and the octane number

Table 7. C_7^+ Aromatic Optimization Results

restrictions		optimization results
		III
1st reactor input temperature (K)	783.15	788.14
2nd reactor input temperature (K)	783.15	783.69
3rd reactor input temperature (K)	783.15	785.20
4th reactor input temperature (K)	776.15	780.82
H/C molar ratio (mol/mol)	2.12	2.06
regeneration gas inlet temperature (K)	729.86	729.04
regenerator oxygen content (%)	0.06105	0.08
heating load (MW/h)	18.554	21.14
steam consumption (t/h)	9.4	9.86
reactor outlet catalyst coke deposition (kg/kgcat)	0.0247	0.0256
regenerator outlet catalyst coke deposition (kg/kgcat)	0.000536	0.0005
C_7^+ aromatic yield (wt %)	57.85	58.59
aromatic yield (wt %)	61.72	62.66
octane number	99.3	99.77

contribution of these components is not very high, which will lead to the drop of the gasoline octane number.

7. CONCLUSIONS

Based on the EO method, the model for the reaction-regeneration section of countercurrent continuous reforming was established, including the reactor module and the regenerator module, connected with the gas−liquid separation model, the heating furnace model, the compressor model, and the heat exchanger model.

(1) According to the time required by model calibration, simulation calculation, and optimization of the process, the established process model can meet the requirements of RTO.

(2) The calibration of the model can bring the calculated values of the model into better consistency with the actual values.

(3) The optimization calculation results show that setting different objective functions can lead to different optimization results. The resulting optimization results fit the reaction mechanism of the reforming, which can be set for different production plans according to the market demand.

■ ASSOCIATED CONTENT

Ⓢi Supporting Information

The Supporting Information is available free of charge at https://pubs.acs.org/doi/10.1021/acsomega.1c04651.

Additional physicochemical properties, technological parameters, model parameters for oil properties, reaction conditions of the commercial unit, composition of feeds and products (PDF)

■ AUTHOR INFORMATION

Corresponding Author

Hongbo Jiang − *Research Institute of Petroleum Processing and International Joint Research Center of Green Energy Chemical Engineering, East China University of Science and Technology, Shanghai 200237, China;* ⓞ orcid.org/0000-

0002-3025-682X; Email: hbjiang@ecust.edu.cn; Fax: 86-21-64252816

Authors

Zhenming Li − Research Institute of Petroleum Processing and International Joint Research Center of Green Energy Chemical Engineering, East China University of Science and Technology, Shanghai 200237, China

Yun Sun − Research Institute of Petroleum Processing and International Joint Research Center of Green Energy Chemical Engineering, East China University of Science and Technology, Shanghai 200237, China

Shubao Jiang − Research Institute of Petroleum Processing and International Joint Research Center of Green Energy Chemical Engineering, East China University of Science and Technology, Shanghai 200237, China

Jianhui Tian − Petro-Cyber Works Information Technology Co., Ltd, Beijing 100007, China

Complete contact information is available at:
https://pubs.acs.org/10.1021/acsomega.1c04651

Notes

The authors declare no competing financial interest.

■ ACKNOWLEDGMENTS

■ NOMENCLATURE

F = molar flow rate, kmol/h

r = reactor radius, m

L = catalyst bed height, m

ρ_b = catalyst bulk density, kg/m^3

r(j) = reaction rate in the reactor, kmol/(kg catalyst·h)

P = reactor pressure, MPa

g = constant of gravity, N/kg

ε = void fraction of the catalyst bed, %

μ = gas viscosity, pa·s

U = apparent velocity, m/s

Φ = particle shape coefficient, 1

d_p = equivalence diameter of the catalyst, m

ρ_f = gas density, kg/m^3

T = reaction temperature, K

Cp = heat capacity of the fraction, kJ/(mol·K)

H = reaction heat of the fraction, kJ/mol

r_{coke} = coke deposition rate, kg coke/ (kg catalyst·h)

E_N = coke-formation activation energy of N&A, kJ/mol

E_P = coke-formation activation energy of P, kJ/mol

$k_{0,coke,N}$ = coke-formation pre-exponential factor for N&A, kg coke/ (kg catalyst·h)

$k_{0,coke,P}$ = coke-formation pre-exponential factor for P, kg coke/ (kg catalyst·h)

P(i) = partial pressure of the ith component, Mpa

$R(\tau)$ = internal residual at the collocation or boundary point

Z_i = state variables of the ith component

δi = interpolation of the ith component

C_C = mass fraction of the carbon in coke

r_C = rate of carbon combustion, kg/(kg·min^{-1})

S = cross-sectional area, m^2

F_s = circulation rate of the catalyst, kg/min

H_H = mass fraction of hydrogen in coke

r_H = rate of hydrogen combustion, kg/(kg·min^{-1})

z = position of the collocation point in the axial direction

F_{O_2} = molar flow rate of oxygen, kmol/min

F_{CO_2} = molar flow rate of carbon dioxide, kmol/min

F_{H_2O} = molar flow rate of steam, kmol/min

x = position of the collocation point in the radial direction

r_{O_2} = reaction rate of oxygen, kmol/(kg·min^{-1})

r_{CO_2} = reaction rate of carbon dioxide, kmol/(kg·min^{-1})

r_{H_2O} = reaction rate of steam, kmol/(kg·min^{-1})

r_0 = radius of the outlet screen, m

r_4 = radius of the inlet screen, m

G_s = mass flow rate of the catalyst of per unit cross-sectional area, kg/(min/m^2)

Cp_s = specific heat capacity of the catalyst, kJ/kg

G_g = molar flow rate of the regeneration gas of per unit cross-sectional area, kmol/(min/m^2)

Cp_g = specific heat capacity of the regeneration gas, J/(mol·K^{-1})

ΔH_C = reaction heat of coke combustion, kJ/mol

ΔH_H = reaction heat of hydrogen combustion, kJ/mol

R_x = residual in the x direction of the regenerator

R_z = residual in the z direction of the regenerator

$f_x(z,x)$ = differential expression in the x direction of the regenerator

$f_z(z,x)$ = differential expression in the z direction of the regenerator

D_{li} = parameter matrix

B_{jk} = parameter matrix, transposed matrix of D_{li}

R = gas constant, J/(mol·K)

L_F = molar flow rate of the liquid phase, kmol/h

V_F = molar flow rate of the gas phase, kmol/h

x_{Fi} = molar fraction of the ith component in the liquid phase, %

y_{Fi} = molar fraction of the ith component in the gas phase, %

z_{Fi} = molar fraction of the ith component in the feeding material, %

p_{Fi}^0 = saturated vapor pressure, Mpa

p_s = separation tank pressure, Mpa

L_{total} = total molar flow rate in the liquid phase, kmol/h

V_{total} = total molar flow rate in the gas phase, kmol/h

k_{Fi} = phase equilibrium constant

L_{Fi} = molar flow rate of the ith component in the liquid phase, kmol/h

V_{Fi} = molar flow rate of the ith component in the gas phase, kmol/h

η_H = efficiency of the heating furnace, %

q_1 = exhaust heat loss, %

q_2 = heat loss of incomplete combustion, %

q_3 = surface heat-dissipation loss, %

α = overheated air coefficient

tg = exhaust temperature, °C

HO_2 = oxygen concentration of smoke gas, %

HCO = carbon monoxide concentration of smoke gas, %

Q_{total} = total heat provided by the fuel, MJ/h

F_{fg} = fuel flow rate, Nm^3/h

Q_{sf} = low calorific value of the unit fuel, MJ/Nm^3

Q_H = heat consumption of the heating process medium, MJ/h

T_{Fin} = inlet temperature of the heating furnace, K

T_{Fout} = outlet temperature of the heating furnace, K

Q_w = heat for steam production, MJ/h

H_w^θ = standard enthalpy of feeding water, kJ/kg

H_G^θ = standard enthalpy of steam, kJ/kg

L_w = flow rate of feeding water, t/h

L_G = steam flow rate, t/h

Q_{sur} = surface heat loss, MJ/h
Q_{eff} = effective heating load, MJ/h
k_{He} = adiabatic index of the eth component
k_H = adiabatic index
y_{He} = volume fraction of the eth component
m_h = polytropic index
T_{Ein} = inlet temperature of the compressor, °C
T_{Eout} = outlet temperature of the compressor, °C
P_1 = inlet hydrogen pressure of the compressor, Mpa
P_2 = outlet hydrogen pressure of the compressor, Mpa
V_1 = inlet hydrogen flow rate of the compressor, Nm^3/h
ε_c = compression ratio
N = theoretical compressor power, KW
N_s = shaft power of the compressor, KW
η_p = polytropic efficiency, %
η_g = mechanical efficiency, %
η_e = transmission efficiency, %
η_i = turbine efficiency, %
G_E = steam consumption, t/h
ΔH_s = enthalpy difference of steam, kJ/kg
Q_{ex} = heat-transfer load, kJ/h
W_h = mass flow rate of hot flow, kg/h
W_c = mass flow rate of cold flow, kg/h
$H_{h,1}$ = enthalpy of the hot fluid at the inlet of the heat exchanger, kJ/kg
$H_{h,2}$ = enthalpy of the hot fluid at the outlet of the heat exchanger, kJ/kg
$H_{c,1}$ = enthalpy of the cold fluid at the inlet of the heat exchanger, kJ/kg
$H_{c,2}$ = enthalpy of the cold fluid at the outlet of the heat exchanger, kJ/kg
AS = heat-transfer area, m^2
K_{gross} = heat-transfer coefficient, W/(m^2·K)
ΔT_{LMTD} = average logarithmic temperature difference of the heat exchanger, K
Δt_h = temperature difference of the hot end, K
Δt_c = temperature difference of the cold end, K
RON = research octane number
k_{RON} = octane correlation coefficient where its value is 1
a_i = effective octane number of the ith component
P_{total} = saturated vapor pressure of the fraction, Kpa
B_{bp} = end boiling-point constant, °C
k_{Ebp} = end boiling-point coefficient of the ith component
Ebp = end boiling point, °C
ρ_{total} = density of fraction, kg/m^3
k_ρ = density coefficient of the ith component
Δ_ρ = density calculation correction coefficient where its value is 8 kg/m^3
VV_{Di} = temperature difference between two adjacent cutting points in real boiling-point distillation, °C
WW_{Di} = temperature difference between two adjacent cutting points in simulated distillation, °C
TBP = distillation temperature of real boiling point, °C
SD = simulated distillation temperature, °C
ASTM = ASTM D86 distillation temperature, °C
f_{ca} = objective function of model calibration
$Y_{F,i}$ = weight coefficient for the molar flow rate of the ith component
Y_T = weight coefficient for the temperature
Y_w = weight coefficient for the coke deposition
$g_i(\vec{x})$ = ith equality constraint
$h_j(\vec{x})$ = jth inequality constraint

W_i = mass percentage of the ith component, wt %

ABBREVIATIONS USED

A aromatics
nP n-paraffins
iP iso-paraffins
5N$_6$ methyl cyclopentane
6N$_6$ cyclohexane
N naphthenes
O olefins

REFERENCES

(1) Degnan, T. F. Chemical reaction engineering challenges in the refining and petrochemical industries—the decade ahead. *Curr. Opin. Chem. Eng.* **2015**, *9*, 75−82.
(2) Meng, W. X.; Banerjee, S.; Zhang, X.; Agarwal, R. K. Process simulation of multi-stage chemical-looping combustion using Aspen Plus. *Energy.* **2015**, *90*, 1869−1877.
(3) Leonzio, G. Process analysis of biological Sabatier reaction for bio-methane production. *Chem. Eng. J.* **2016**, *290*, 490−498.
(4) Lambert, C.; Laulan, B.; Decloux, M.; Romdhana, H.; Courtois, F. Simulation of a sugar beet factory using a chemical engineering software (ProSimPlus) to perform Pinch and exergy analysis. *J. Food. Sci.* **2018**, *225*, 1−11.
(5) Kökdemir, B.; Acaralı, N. A novel study on CHEMCAD simulation of isopropyl alcohol dehydrogenation process development. *J. Indian. Chem. Soc.* **2021**, *98*, No. 100035.
(6) Lourderaj, U.; Sun, R.; Kohale, S. C.; Barnes, G. L.; de Jong, W. A.; Windus, T. L.; Hase, W. L. The VENUS/NWChem software package. Tight coupling between chemical dynamics simulations and electronic structure theory. *Comput. Phys. Commun.* **2014**, *185*, 1074−1080.
(7) Gao, N.; Zhai, C.; Sun, W.; Zhang, X. Equation oriented method for Rectisol wash modeling and analysis. *Chin. J. Chem. Eng.* **2015**, *23*, 1530−1535.
(8) Casella, F.; Bartolini, A. G.; Leva, A. Equation-Based Object-Oriented modelling and simulation of large-scale Smart Grids with Modelica. *IFAC-PapersOnLine* **2017**, *50*, 5542−5547.
(9) Hagen, B. A. L.; Agromayor, R.; Nekså, P. Equation-oriented methods for design optimization and performance analysis of radial inflow turbines. *Energy* **2021**, *237*, No. 121596.
(10) Bizon, N.; Thounthong, P. Real-time strategies to optimize the fueling of the fuel cell hybrid power source: A review of issues, challenges and a new approach. *Renew. Sustainable Energy Rev.* **2018**, *91*, 1089−1102.
(11) Kumar, V.; Kaistha, N. Real-Time Optimization of a Reactor−Separator−Recycle Process II: Dynamic Evaluation. *Ind. Eng. Chem. Res.* **2019**, *58*, 1966−1977.
(12) Galan, A.; Prada, C. D.; Gutierrez, G.; Sarabia, D.; Gonzalez, R.; Sola, M.; Marmol, S. Validation of a hydrogen network RTO application for decision support of refinery operators. *IFAC-PapersOnLine* **2018**, *51*, 73−78.
(13) Hernandez, R.; Dreimann, J.; Vorholt, A.; Behr, A.; Engell, S. Iterative Real-Time Optimization Scheme for Optimal Operation of Chemical Processes under Uncertainty: Proof of Concept in a Miniplant. *Ind. Eng. Chem. Res.* **2018**, *57*, 8750−8770.
(14) de Gouvêa, M. T.; Odloak, D. One-layer real time optimization of LPG production in the FCC unit: procedure, advantages and disadvantages. *Comput. Chem. Eng.* **1998**, *22*, S191−S198.
(15) Miletic, I. P.; Marlin, T. E. On-line Statistical Results Analysis in Real-Time Operations Optimization. *Ind. Eng. Chem. Res.* **1998**, *37*, 3670−3684.
(16) Won, W.; Lee, K. S.; Lee, S.; Jung, C. Repetitive control and online optimization of Catofin propane process. *Comput. Chem. Eng.* **2010**, *34*, 508−517.
(17) Mercangöz, M.; Doyle, F. J. Real-time optimization of the pulp mill benchmark problem. *Comput. Chem. Eng.* **2008**, *32*, 789−804.

(18) Lid, T.; Strand, S. Real-time optimization of a cat cracker unit. *Comput. Chem. Eng.* **1997**, *21*, S887−S892.

(19) Xenos, D. P.; Cicciotti, M.; Kopanos, G. M.; Bouaswaig, A. E. F.; Kahrs, O.; Martinez-Botas, R.; Thornhill, N. F. Optimization of a network of compressors in parallel: Real Time Optimization (RTO) of compressors in chemical plants − An industrial case study. *Appl. Energy* **2015**, *144*, 51−63.

(20) Zhou, X.; Hou, Z.; Wang, J.; Fang, W.; Ma, A.; Guo, J.; Klein, M. T. Molecular-Level Kinetic Model for C12 Continuous Catalytic Reforming. *Energy Fuel* **2018**, *32*, 7078−7085.

(21) Pontes, K. V.; Wolf, I. J.; Embiruçu, M.; Marquardt, W. Dynamic Real-Time Optimization of Industrial Polymerization Processes with Fast Dynamics. *Ind. Eng. Chem. Res.* **2015**, *54*, 11881−11893.

(22) Wei, M.; Yang, M.; Qian, F.; Du, W.; He, W.; Zhong, W. Dynamic Modeling and Economic Model Predictive Control with Production Mode Switching for an Industrial Catalytic Naphtha Reforming Process. *Ind. Eng. Chem. Res.* **2017**, *56*, 8961−8971.

(23) Krishnamoorthy, D.; Jahanshahi, E.; Skogestad, S. Feedback Real-Time Optimization Strategy Using a Novel Steady-state Gradient Estimate and Transient Measurements. *Ind. Eng. Chem. Res.* **2019**, *58*, 207−216.

(24) Li, H.; Ma, C.; Zou, X.; Li, A.; Huang, Z.; Zhu, L. On-board methanol catalytic reforming for hydrogen Production-A review. *Int. J. Hydrogen Energy* **2021**, *46*, 22303−22327.

(25) Esmaili, H.; Kazeminejad, H.; Khalafi, H. Prediction of temperature distribution in annular fuels using orthogonal collocation method. *Ann. Nucl. Energy* **2019**, *134*, 77−87.

(26) Gallucci, F.; De Falco, M.; Tosti, S.; Marrelli, L.; Basile, A. Co-current and counter-current configurations for ethanol steam reforming in a dense Pd−Ag membrane reactor. *Int. J. Hydrogen Energy* **2008**, *33*, 6165−6171.

(27) Babaqi, B. S.; Takriff, M. S.; Kamarudin, S. K.; Othman, N. T. A. Mathematical modeling, simulation, and analysis for predicting improvement opportunities in the continuous catalytic regeneration reforming process. *Chem. Eng. Res. Des.* **2018**, *132*, 235−251.

(28) Ancheyta-Juárez, J.; Villafuerte-Macías, E. Kinetic Modeling of Naphtha Catalytic Reforming Reactions. *Energy Fuel* **2000**, *14*, 1032−1037.

(29) Jiang, H.; Sun, Y.; Jiang, S.; Li, Z.; Tian, J. Reactor Model of Counter-Current Continuous Catalyst-Regenerative Reforming Process toward Real Time Optimization. *Energy Fuel* **2021**, *35*, 10770−10785.

(30) Yusuf, A. Z.; John, Y. M.; Aderemi, B. O.; Patel, R.; Mujtaba, I. M. Modelling, simulation and sensitivity analysis of naphtha catalytic reforming reactions. *Comput. Chem. Eng.* **2019**, *130*, No. 106531.

(31) Cruz, B. M.; da Silva, J. D. A two-dimensional mathematical model for the catalytic steam reforming of methane in both conventional fixed-bed and fixed-bed membrane reactors for the Production of hydrogen. *Int. J. Hydrogen Energy* **2017**, *42*, 23670−23690.

(32) Jiang, S.; Jiang, H.; Li, Z.; Tian, J. Real-Time Optimization Model for Continuous Reforming Regenerator. *China. Pet. Process. Petrochem. Technol.* **2021**, *23*, 90−103.

(33) Zhou, J.; Zhao, J.; Zhang, J.; Zhang, T.; Ye, M.; Liu, Z. Regeneration of catalysts deactivated by coke deposition: A review. *Chin. J. Catal.* **2020**, *41*, 1048−1061.

(34) Feliu-Batlle, V.; Rivas-Perez, R. Control of the temperature in a petroleum refinery heating furnace based on a robust modified Smith predictor. *ISA Trans.* **2021**, *112*, 251−270.

(35) Enterprise Standard of China National Petroleum Corporation: Monitoring and testing method for energy saving of heating furnace in petrochemical process: Q/Y50-2002[S].

(36) Zhao, D.; Hua, Z.; Dou, M.; Huangfu, Y. Control oriented modeling and analysis of centrifugal compressor working characteristic at variable altitude. *Aerosp. Sci. Technol.* **2018**, *72*, 174−182.

(37) Sarfraz, O.; Bach, C. K.; Bradshaw, C. R. A novel technique for computationally efficient consideration of cross-fin conduction in fin-and-tube heat exchanger models. *Int. J. Refrig.* **2019**, *107*, 73−83.

(38) Dias, T.; Oliveira, R.; Saraiva, P.; Reis, M. S. Predictive analytics in the petrochemical industry: Research Octane Number (RON) forecasting and analysis in an industrial catalytic reforming unit. *Comput. Chem. Eng.* **2020**, *139*, No. 106912.

(39) Tao, Y. L.; Wang, S. H.; Zhou, X. D.; Cao, W. F.; Yu, X. B. Study on the determination method of octane value of coal direct liquefaction catalytic reforming product oil. *China Coal* **2014**, *40*, 425−428+432.

(40) Yuan, X.; Sun, M.; Wang, C.; Zhu, X. Full temperature range study of rice husk bio-oil distillation: Distillation characteristics and product distribution. *Sep. Purif. Technol.* **2021**, *263*, No. 118382.

(41) Saeedi, R.; Iranshahi, D. Multi-objective optimization of thermally coupled reactor of CCR naphtha reforming in presence of SO2 oxidation to boost the gasoline octane number and hydrogen. *Fuel* **2017**, *206*, 580−592.